POAC'15
Trondheim, Norway

Proceedings of the 23rd International Conference on
Port and Ocean Engineering under Arctic Conditions
June 14-18, 2015
Trondheim, Norway

MECHANISMS OF INTERACTION BETWEEN MESOSCALE OCEAN EDDIES AND SEA ICE IN HIGH-RESOLUTION ICE-OCEAN COUPLED MODEL OF THE LAPTEV SEA IN SUMMER

Liyanarachchi Waruna Arampath De Silva [1,2], and Hajime Yamaguchi [2]
[1] National Institute of Polar Research, Tokyo, Japan
[2] The University of Tokyo, Kashiwa, Japan

ABSTRACT

Precise ice distribution prediction is one of key issues to realize safe and efficient navigation in the Northern Sea Route (NSR). Results of high-resolution (2.5km) hindcast computation (De Silva, 2015) have shown good agreement with observational ice distribution, which has motivated us to search for possible factors driving the sea ice variability in NSR using numerical model. We have found that mesoscale eddy production is one of the main factors responsible for sea ice variability in the Laptev Sea marginal ice zones. A three-dimensional high-resolution ice-ocean coupled model is used to investigate the eddy generation mechanisms. The model is designed to represent a typical condition for the summertime Laptev Sea mixed layer. Eddy generation due to ice-ocean interaction is discussed in details; a wind stress is larger over the ice than that on open water and induces Ekman pumping and suction, which produce dipole eddy motions. Vertical motions associated with the dipole eddies lead to deep vertical mixing and the subsequent melting of the ice. The dipole eddies generated by barotropic instability is further enhanced by vertical mixing and freshwater input due to sea ice melt. Those eddies are important to exchange the heat across the ice edge and to meandering of ice edge. Numerical sensitivity experiments suggest that the horizontal scale of generated eddies depends on the surface forcing. Also, these small-scale features are not modeled well with horizontal grids coarser than approximately 5 km.

INTRODUCTION

Retreat of summer sea ice in the Arctic Ocean continues to attract interest in exploring Arctic areas, such as the exploitation of natural resources and commercial shipping through Arctic sea routes (ASR). To navigate in the ASRs, we need precise ice distribution predictions along the sea routes. However, ocean general circulation models have difficulties in predicting the sea ice distribution, temperature and salinity profile in the Arctic Ocean. One main possibility of such difficulties is that small-scale processes in both sea ice and ocean mixed layers are not resolved explicitly but are just parameterized.

Results of high-resolution (2.5km) hindcast computation in the Laptev Sea (De Silva, 2015) have shown good agreement with the observational sea ice distribution, which has motivated us to search for possible factors driving the sea ice variability in the Northern Sea Route (NSR) using high-resolution numerical model. We have found that the mesoscale eddy production is one of the main factors responsible for sea ice variability in the NSR marginal ice zones (MIZ). Observational evidence of mesoscale eddies in the Eurasians basin (Woodgate et al., 2001) and in the Laptev Sea (Dmitrenko et al., 2008) also confirms the existence and importance of mesoscale eddies in NSR.

Many mesoscale eddy generation mechanisms, based on observational and modeling studies, have been suggested in the marginal ice zones. Which are, current instability due to

baroclinic instability (Griffiths and Linden, 1981; Wadhams and Squire, 1983) and barotropic instability (Johannessen et al., 1983), current-eddy interaction (Stern and Flierl, 1987), topographic steering and trapping due to conservation of potential vortices (Johannessen et al., 1987), and ice edge air-ocean interaction (Häkkinen, 1986; Ikeda, 1990).

Some researchers also extended their work to analyzing the ice-edge meandering due to mesoscale eddies (Ikeda, 1990; Johannessen et al., 1983). They have suggested that among the above-mentioned five eddy generation mechanisms, the ice edge air-ocean interaction will play a significant role in generation of dipole eddies and meandering of the ice edge in MIZ. Upwelling/ downwelling and associated eddies can be driven by winds at the ice-edge. Because air-ice-ocean coupling is stronger than air-ocean coupling, the Ekman response is larger under the ice than open water.

However, previous numerical works (Ikeda, 1990) used two-layer models with excluded thermodynamics effects to explain the dipole eddies and ice meandering. They also simplified the sea ice edge with Gaussian distribution and exclude the internal stress of sea ice. Those simplifications somewhat overestimate the sea ice deformations under the influence of dipole eddies. Also in the previous studies, modification of ocean stratification under the wind-generated ice-edge eddies and their feedbacks on sea ice movements are not taken into account.

Therefore, in the present paper we have discussed the characteristic of ice-edge eddies due to air-ocean interaction in the MIZ and their contribution to melting, deforming, movements of sea ice, and modifying the underneath ocean stratification and ocean currents. To investigate these effects we use the numerical modelling approach with three-dimensional ice-ocean coupled model. By varying spatial grid size, we also evaluate the how grid resolution affects the characteristics of mesoscale eddies and sea ice in the MIZ.

MODEL DESCRIPTION

A high-resolution three-dimensional ice-ocean coupled model (ice-POM) is used to investigate the mesoscale eddy generation due to the ice edge air-ocean interaction and its' impact on sea ice. The ocean model is based on the Princeton Ocean Model (Mellor et al., 2002). The hydrostatic and Boussinesq approximations are used. We also used the second-order accuracy, sign-preserving tracer advection scheme, Multidimensional Positive Definite Advection Transport Algorithm (MPDAT) (Smolarkiewicz, 1984). The ice rheological model is based on the elastic-viscous-plastic (EVP) rheology proposed by Hunke and Dukowicz (1997) and is modified with ice floe collisions taken into account, following Sagawa & Yamaguchi (2006) and Sagawa (2007). The ice thermodynamics model is based on the 0-layer thermodynamic model proposed by Semtner (1976). Physical constant and model parameters used in the ice-POM model are given in Table 1.

The horizontal size of the model domain is 667 km × 667 km and depth of the domain is 500 m. The horizontal grid size is 1 km and vertical layer thickness is 1m in the upper 100 m and linearly increases to the bottom. At the lateral boundaries, radiation boundary condition is used and at the bottom free-slip boundary condition is used. The latitude is set at 70°N, and an *f*-plane approximation is used.

Initially, circular ice patch with 100 km radius, 100% concentration and 1 m thickness is placed on the ocean surface and ice patch's center at the (150 km, 333 km) x-y plane. Initial ice patch and ocean are at rest. Ocean salinity and temperature are horizontally uniform and have a vertical profile characteristic of the summer-time Laptev Sea, where a halocline separates the fresh mixed layer near the surface from the warm dense water below as shown in figure 1. We approximate the vertical profiles using hyperbolic-tangent curve (inflection point at the 40m depth). Salinity and temperature are 30 psu and freezing point (-1.6 °C) at the surface mixed layer, and 32 psu and 1.6 °C below the halocline and thermocline.

Table 1. Model Parameters

Symbol	Description	Value
dt_{ext}	time step in external mode	3 seconds
dt_{int}	time step in internal mode and thermodynamics mode	60 seconds
C_{Dai}	air-ice drag coefficient	2.4×10^{-3}
C_{Daw}	air-water drag coefficient	1.2×10^{-3}
C_{Diw}	ice-water drag coefficient	7.2×10^{-3}
C_h	ice-ocean heat transfer coefficient	5.0×10^{-3}
C_p	specific heat of sea water	4000 J $kg^{-1}K^{-1}$
f	Coriolis parameter	1.37×10^{-4} s^{-1}
g	Gravitational acceleration	9.80 m s^{-2}
ρ_w	density of sea water	1025.9 kg m^{-3}

Ice patch is then forced by spatially uniform westerly wind with magnitude 10 ms^{-1}. The wind is slowly ramped to 10 ms^{-1} in 5 days using a sinusoidal function and held constant for another 5 days, after which the wind ceases. The calculation is carried out for 40 days after wind cessation.

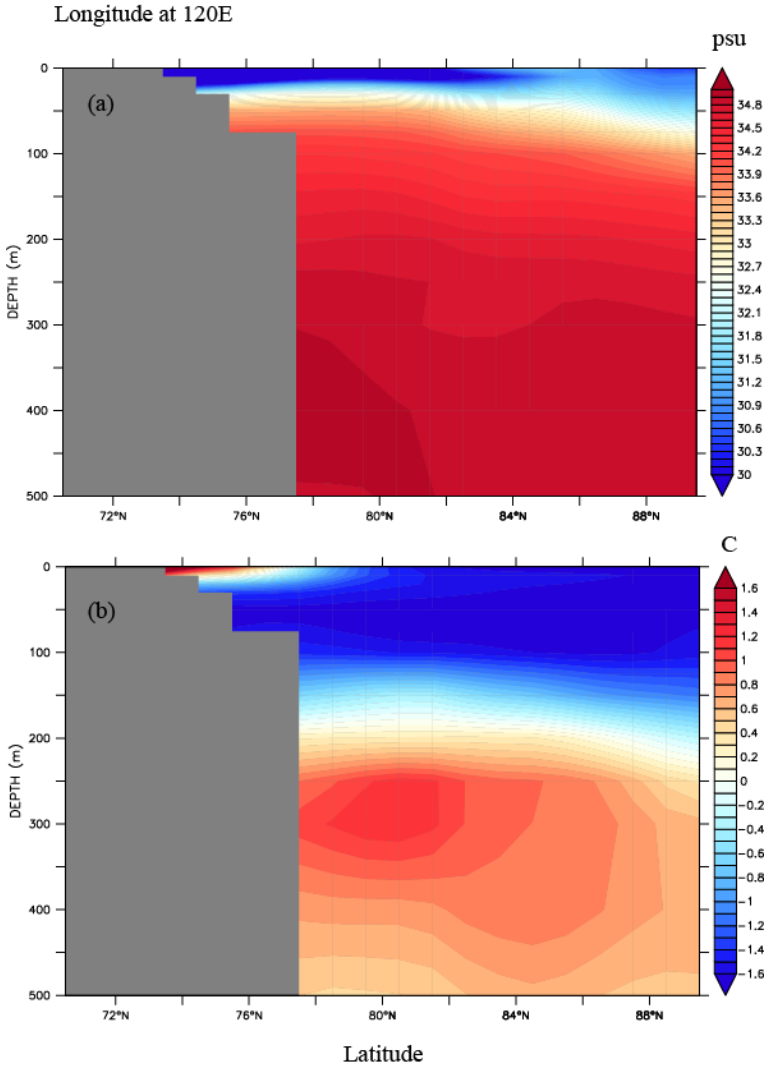

Figure 1. Vertical profile at 120E longitude (a) salinity (b) temperature PHC climatological data on August

In order to focus on ice-ocean interaction and self-melt process of sea ice under mesoscale eddies, we exclude the ice and ocean surfaces heat and buoyancy fluxes. However, ice-ocean bottom interface heat flux is given by:

$$H_{iw} = \rho_w C_p c_h \sqrt{\frac{\tau_w}{\rho_w}} \left(T_m - T_{mf} \right) \tag{1}$$

where T_m is the mixed-layer temperature, T_{mf} is the mixed-layer freezing temperature and τ_w is sea surface stress.

We have used the freshwater tracer to investigate the transport process of freshwater supplied by melting sea ice.

RESULTS AND DISCUSSIONS

Under the influence of wind, ice patch moves to positive x direction with speed of about 0.27 ms^{-1} and negative y direction with speed of about 0.056 ms^{-1}. Under the influence of wind, anticyclonic and cyclonic eddies are developed on the right and left of the ice patch, respectively, when looking down in the downwind direction. Generated eddies and ice patch are advected with the mean flow to the downstream. After the wind cessation, dipole eddies itself drive the ice patch in the northeast direction. By day 28, three cyclonic eddies with radii 14, 17 and 36 km and one anticyclonic eddy with radius 17 km are seen in the upper ocean, figure 2. Rossby radius of deformation R_d= 4.47 km in the region therefore produced eddies are 3 to 8 times larger than Rossby radius.

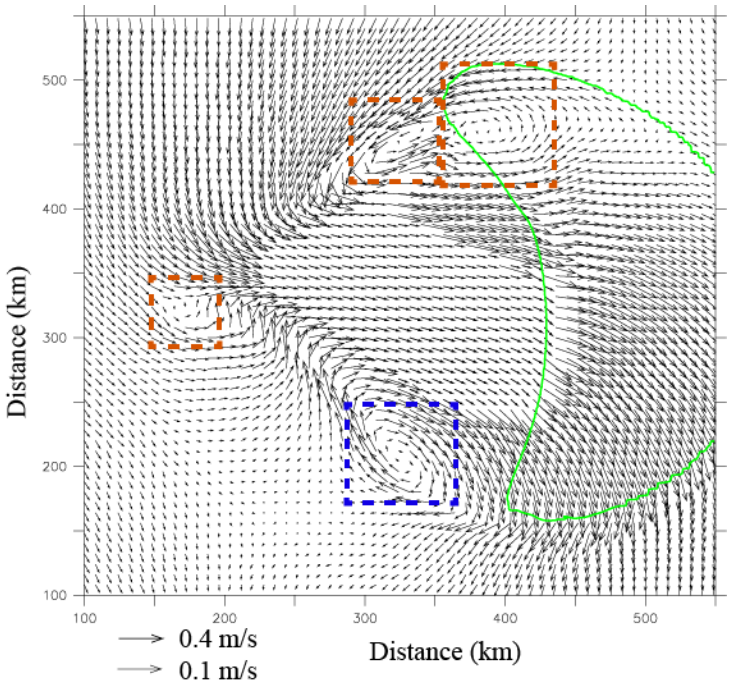

Figure 2. Surface ocean velocity vector on day 28. Red rectangles show cyclonic eddy locations and blue rectangle shows anticyclonic eddy location. Green contour shows ice edge position.

Ice-edge eddy generation mechanism

Eddy generation due to the ice edge upwelling and downwelling has been extensively studied by many researchers (Häkkinen, 1986; Ikeda, 1990). The generation mechanism of these eddies can be described as follows. Initially, the wind stress acting on the water under the ice is much larger than over open ocean due to the different drag coefficients. Therefore,

Ekman transport is convergence and divergence at the right and left edge of the ice patch, respectively, when looking down in the downwind direction. This convergence and divergence generate the barotropic dipole eddies. Since the Laptev Sea pycnocline is very shallow, Ekman transport associated upwelling brings the warm and heavy bottom water to the surface. The vertical upwelling (cyclonic eddy) produces an upward heat flux, resulting in enhancing melting of sea ice near the ice edge. Then this ice-melted cold and freshwater is accumulated under the anticyclonic eddy and downwelling into the mixed layer. These processes restratified the mixed layer and generate the local oceanic fronts. Localized mixing caused by Ekman driven convection at the front results in additional circulation. This circulation leads to the formation of baroclinic mesoscale eddies after the wind cessation as shown in figure 2.

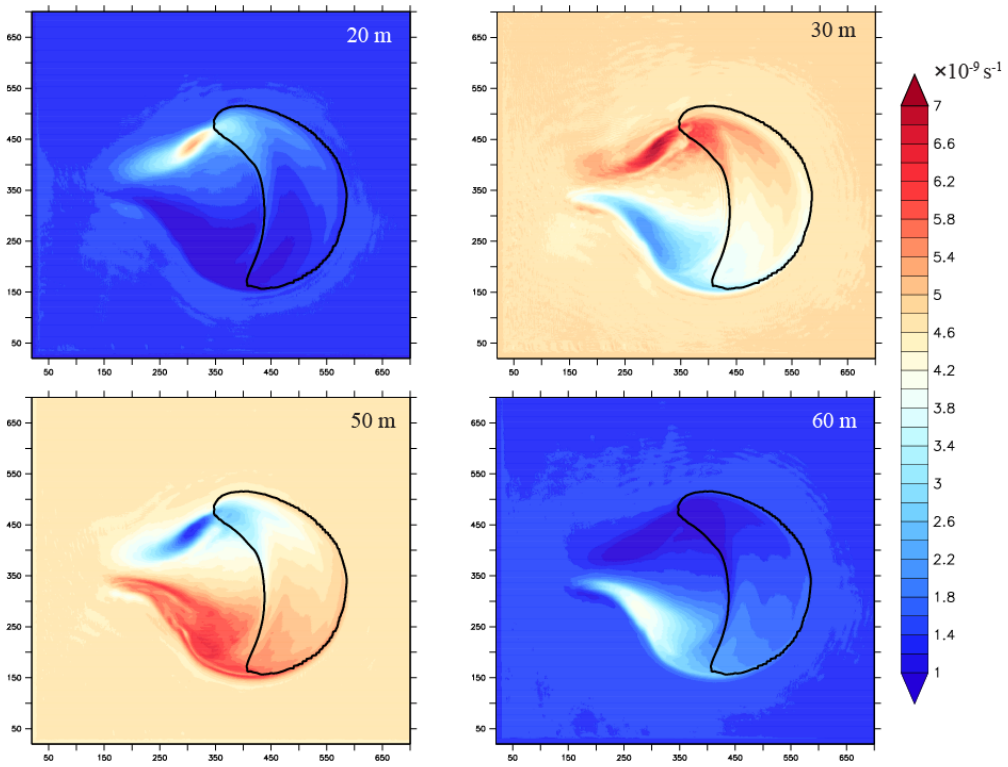

Figure 3. Potential vorticity (PV) [10^{-9} s^{-1}] distributions at various depths (20m, 30m, 50m, and 60m) after 28 days of simulation. Black contour shows ice edge location.

By looking at the potential vorticity (PV) distribution, we can discuss the frontal formation and baroclinic eddies. PV is defined as,

$$PV = \omega_a \cdot \nabla b \tag{2}$$

where $\omega_a = f\mathbf{k} + \nabla \times \mathbf{u}$ is the absolute vorticity (f is the Coriolis parameter, $\mathbf{k}$ is the vertical unit vector, and $\mathbf{u}$ is the velocity); $b = -g\rho/\rho_\circ$ is the buoyancy (g is the gravitational acceleration, ρ is the density, and ρ_0 is a reference density).

Due to the strong halocline in the model domain (as shown in figure 1) depths at 30m and 50m shows the high PV compared to the 20m and 60m in figure 3. As shown in figure 3 the localized streams of high PV fluid at the halocline is drawn to the surface by the Ekman upwelling. While low PV surface fluid is subducted into the interior halocline. In the layer at 30 m depth, two distinct high PV anomalies are shown (in figure 3). One is under the ice patch and one is next to the ice edge. High and low PV anomalies also show the cyclonic and

anticyclonic eddy paths. It's also very clear that PV anomalies under the cyclonic eddy is more concentrated and shows a narrow horizontal distribution while anticyclonic PV anomaly shows wider horizontal distribution.

Ice deformations

Time series of the ice edge locations are shown in figure 4(a). Under the influence of wind force 10 day, the ice patch is advected about 200 km to the downwind direction. After the wind cessation, ice patch travelled about 50 km in the downwind direction during 20 days. On the other hand, after the wind cessation, ice patch is greatly undergoing to the deformation process by generated dipole mesoscale eddies and formed the arc shape ice bunch. This arc shape ice edge agrees well with the observations based on satellite images in the Labrador and Newfoundland shelves (Ikeda, 1990) and based on numerical model in the Laptev Sea (De Silva, 2015).

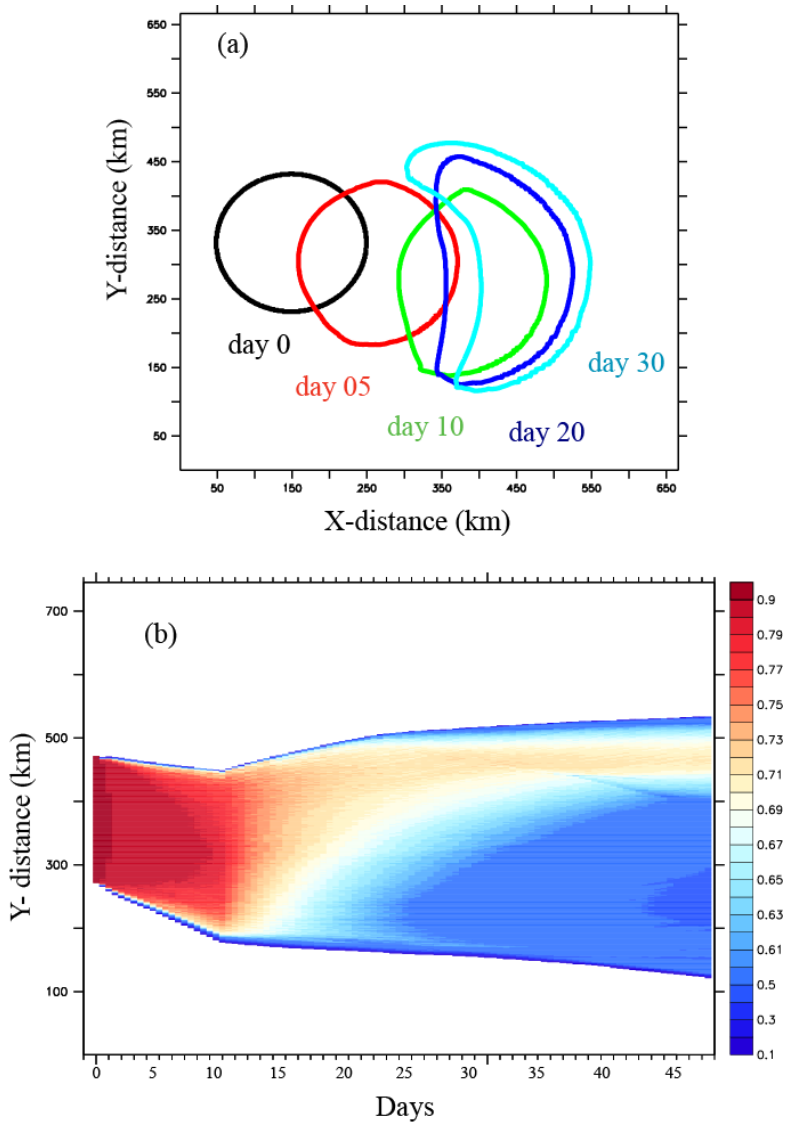

Figure 4. Time series of (a) ice edge (concentration equal to 0.1) locations (b) ice concentration (area average in x direction)

Time series of spatial sea ice concentration distribution is shown in figure 4(b). Under the cyclonic eddy, sea ice is accumulated in north and increases the sea ice concentration while under the influence of anticyclonic eddies sea ice is dissipated in south and decreases the sea ice concentration. Although the figures are omitted, it is also seen that under the influence of wind forcing mean surface ocean current disturbs the eddies appear on the ocean surface. And ice bunch is freely advected with the mean flow. After the wind cessation, surface layer eddy structure is emerged and starts to deform the circular ice bunch shape into the arc shape. The arc shape area is much larger than the original circular area; therefore it reduces the whole ice patch concentration. But on top of the cyclonic eddies sea ice is accumulated in the eddy core due to the radial inward pressure.

Ice-melted freshwater distribution

To investigate the vertical freshwater transport, we divide the domain vertically into six layers. The thickness of the each layer is 10 m. As shown in figure 5, during the wind forcing (up to day 10) about 40% of ice-melted freshwater is accumulated in layer 0-10 m, about 25% is accumulated in layer 10-20m, layer 20-30 m also accumulated the 25%, in 30-40 m layer 8% is accumulated and deeper than 40 m there is no freshwater accumulated. After the wind is ceased, 0-10 m layer freshwater accumulation is gradually increased up to 63% and 10-20 m layer gradually decreased up to 17% and 20-30 m layer decreased up to 10% and 40-50m layer increased up to 2% and 50-60 m layer increased less than 1%. Since the top of the halocline is at 30 m, this vertical profile suggests that 90% freshwater is distributed in mixed surface layer and only 10% is subducted below the halocline. After the wind is ceased, increase of freshwater in the 0-10 m layer (about 23%) also suggests that mesoscale eddies play a significant role in ocean stratification in the mixed layer.

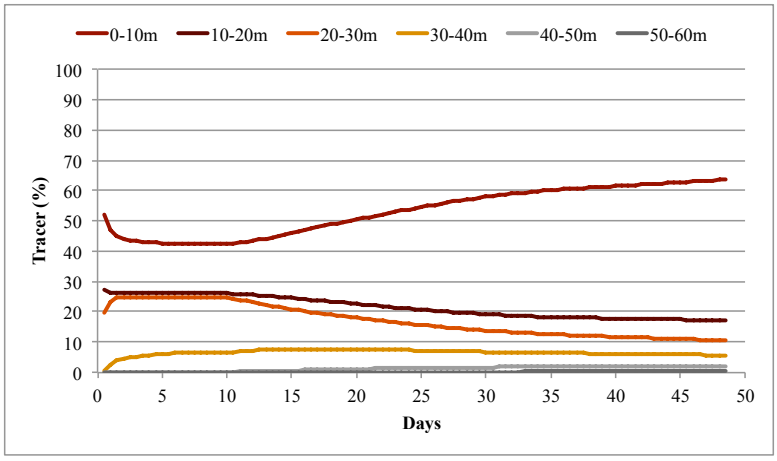

Figure 5. Time series of vertical distribution of the ice melted freshwater tracer [%]

Grid dependency effects

We also investigate the grid size dependence on mesoscale eddy-resolving feature, ice deformation and sea ice bottom melting by changing the horizontal grid sizes, 1, 2.5, 5, and 10 km. The vertical resolution and other model parameters are kept same as standard 1 km experiment. The bottom melting rate is described in equation 1. Since, initial surface ocean temperature is set at freezing point, heat supply from the deeper water only melts the sea ice. Figure 6 shows the bottom melt rate of each grid size after the wind cessation. The 10 km resolution cannot reproduce the bottom melt rate compared to the high-resolution models. 5 km grid size also shows a little discrepancy compare to the 1 km and 2.5 km models.

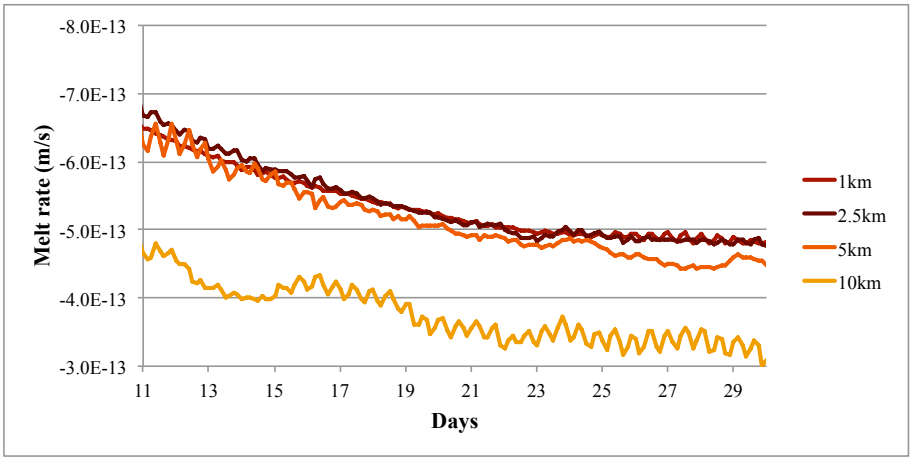

Figure 6. Time series of area average bottom melt rate

We also investigate the effect of grid resolution on the sea ice deformation. A simple quantitative approach based on mean displacement is used for deformation assessment. First, shape of the ice bunch is calculated based on the mean displacement ϕ, as shown in equation 3.

$$\phi = \frac{1}{n}\sum_{i=1}^{n} d_A(P_i, P_c) \tag{3}$$

where P_c is the areal centroid of the ice bunch and d_A is distance from the centroid to ith grid cell. n is the total number of grid cells within the ice bunch. If the two geometric shapes of ice bunches are same, mean displacement ϕ should be equal. Therefore, mean displacement error E with respect to the initial shape of ice bunch gives us a quantitative measure for sea ice deformation. The mean displacement error E is calculated as follows,

$$E = \frac{\left|\phi(T=t) - \phi(T=0)\right|}{\phi(T=0)} \tag{4}$$

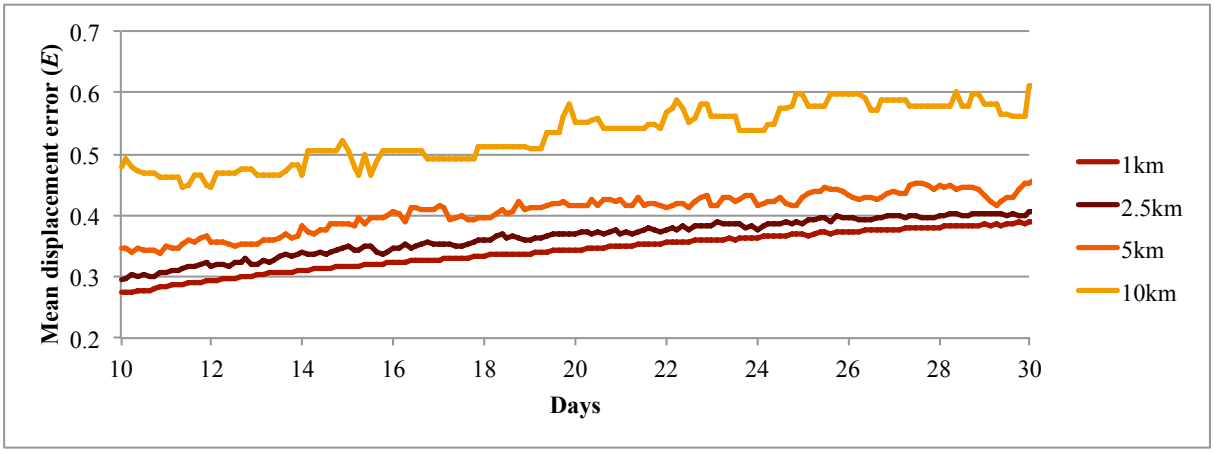

Figure 7. Time series of mean displacement error E

After the wind cessation, time series of mean displacement error are shown in figure 7. Grid resolution of 10 km and 5 km show the high mean displacement errors compared to the 1 and 2.5 km resolution computations. Also, all four grid resolution computations have shown the incremental trend of mean displacement errors compared to their initial circular shapes.

This grid dependency experiments show that the resolving of mesoscale eddies plays a significant role in sea ice melting and deforming of the ice edge.

CONCLUSIONS

The results can be summarized as follows. This paper examines the generation mechanism of the ice edge mesoscale eddies.

When the wind starts blowing on partially ice-covered water, uneven distribution of wind shearing force initiates dipole eddies. Vertical motions associated with the dipole eddies lead to deep vertical mixing and the subsequent melting of the ice. After the wind cessation baroclinic instability becomes dominant due to the density fronts generated by upwelling and downwelling.

Ice-melted freshwater is trapped in the first 10 m layers. The bottom melts and ice edge deformations due to the mesoscale eddy associated upwelling and downwelling are not adequately resolved by horizontal grid size larger than 5 km.

ACKNOWLEDGMENTS

The authors wish to acknowledge the support from the GRENE Network of Excellence Program Arctic Climate Change Research Project. This study is partly supported by a JSPS Grant-in-Aids for Scientific Research A.

REFERENCES

De Silva, L.W.A., Yamaguchi, H., Ono, J., 2015. Ice-ocean coupled computations for sea ice prediction to support ice navigation in the Arctic sea routes. Polar Research. (in press)

Griffiths, R.W., Linden, P.F., 1981. The stability of buoyancy-driven coastal currents. Dyn. Atmos. Ocean. 5, pp. 281–306.

Häkkinen, S., 1986. Coupled ice-ocean dynamics in the marginal ice zones: Upwelling/downwelling and eddy generation. J. Geophys. Res. 91, pp. 819–832.

Hunke, E.C., Dukowicz, J.K., 1997. An Elastic–Viscous–Plastic model for sea ice dynamics. J. Phys. Oceanogr. 27, pp. 1849–1867.

Ikeda, M., 1990. Mesoscale eddy formation and evolution in the ice-covered ocean, in: Proceedings of the Symposium on Ice-Ocean Dynamics and Mechanics. Annals of Glaciology, Hanover, New Hampshire, U.S.A., pp. 139–147.

Johannessen, J.A., Johannessen, O.M., Svendsen, E., Shuchman, R., Manley, T., Campbell, W.J., Josberger, E.G., Sandven, S., Gascard, J.C., Olaussen, T., Davidson, K., Van Leer, J., 1987. Mesoscale eddies in the Fram Strait marginal ice zone during the 1983 and 1984 Marginal Ice Zone Experiments. J. Geophys. Res. 92, pp. 6754–6772.

Johannessen, O.M., Johannessen, J.A., Morison, J., Farrelly, B.A., Svendsen, E.A.S., 1983. Oceanographic conditions in the marginal ice zone north of Svalbard in early fall 1979 with an emphasis on mesoscale processes. J. Geophys. Res. 88, pp. 2755–2769.

Mellor, G.L., Hakkinen, S., Ezer, T., Patchen, R., 2002. A generalization of a sigma coordinate ocean model and an intercomparison of model vertical grids., in: In Ocean Forecasting: Conceptual Basis and Applications. Springer, Berlin Heidelberg, pp. 55–72.

Sagawa, G., 2007. Development of ice dynamic model that takes account of floe collision and its validation in numerical sea ice forecast in the Sea of Okhotsk (in Japanese). The University of Tokyo, Tokyo.

Sagawa, G., Yamaguchi, H., 2006. A Semi-Lagrangian Sea Ice Model For High Resolution Simulation, in: The Sixteenth International Offshore and Polar Engineering Conference. International Society of Offshore and Polar Engineers, San Francisco, California, pp. 584–590.

Semtner, A.J., 1976. A Model for the Thermodynamic Growth of Sea Ice in Numerical Investigations of Climate. J. Phys. Oceanogr. 6, pp. 379–389.

Smolarkiewicz, P.K., 1984. A fully multidimensional positive definite advection transport algorithm with small implicit diffusion. J. Comput. Phys. 54, pp. 325 –362.

Stern, M.E., Flierl, G.R., 1987. On the interaction of a vortex with a shear flow. J. Geophys. Res. 92, pp. 10733–10744.

Wadhams, P., Squire, V.A., 1983. An ice-water vortex at the edge of the East Greenland Current. J. Geophys. Res. 88, pp. 2770–2780.